



Silicon oxynitride platform for linear and nonlinear photonics at NIR wavelengths

GIOELE PICCOLI,^{1,2,*}  MATTEO SANNA,²  MASSIMO BORGHI,^{2,3}  LORENZO PAVESI,²  AND MHER GHULINYAN¹ 

¹*Sensors and Devices, Fondazione Bruno Kessler, via Sommarive 18, 38123 - Trento, Italy*

²*Department of Physics, University of Trento, via Sommarive 14, 38123 - Trento, Italy*

³*Present address: Department of Physics, University of Pavia, via A. Bassi 6, 27100 - Pavia, Italy*

*gpiccoli@fbk.eu

Abstract: The development of versatile and novel material platforms for integrated photonics is of prime importance in the perspective of future applications of photonic integrated circuits for quantum information and sensing. Here we present a low-loss material platform based on high-refractive index silicon oxynitride (SiON), which offers significant characteristics for linear and non-linear optics applications in a wide range of red/near-infrared wavelengths. The demonstrated propagation loss <1.5 dB/cm for visible wavelengths enables the realization of long and intricate circuitry for photon manipulations, as well as the realization of high quality factor resonators. In addition, the proposed SiON shows a high nonlinear index of 10^{-19} m²/W, improving the strength of nonlinear effects exploitable for on-chip photon generation schemes.

© 2022 Optica Publishing Group under the terms of the [Optica Open Access Publishing Agreement](#)

1. Introduction

The development of novel platforms for integrated photonics, characterized by a strong versatility in terms of applications, is of prime importance for the realization of emerging photonics applications in the fields of sensing, metrology, quantum communications and quantum computing [1,2].

Several technologies for photonic integrated circuits (PICs) have been proposed and developed in the last decades. Silicon photonics emerged among the first, exploiting the advanced CMOS manufacturing techniques optimized for microelectronics. Nowadays, Silicon-on-Insulator (SOI) based devices are spreading in the commercial world (see Ref. [3] and references therein). State of the art SOI devices achieve propagation losses of less than 1 dB/cm in the telecom C-Band, offering highly efficient passive components [4–6]. Active components are implemented with two approaches: phase-shifters based on *p-n* junctions are realized directly on the Si waveguides, while photodetectors and light sources require hetero-integration of germanium or III-V compound semiconductors [7–11]. The SOI platform is functional in the spectral range limited to wavelengths longer than $1.1 \mu\text{m}$ (energy bandgap $E_g \sim 1.1$ eV) for linear operations and is characterized by significant excited-carrier (EC) and two-photon absorption (TPA) up to $2.2 \mu\text{m}$ ($\sim E_g/2$) in nonlinear operations.

Silicon Nitride (SiN) has been introduced as an alternative dielectric platform for integrated photonics [12]. It is transparent at wavelengths from 400 nm to $7.0 \mu\text{m}$ (up to $3.0 \mu\text{m}$ if embedded in silica), while very recent developments report on operation in the ultra-violet region [13]. Passive components show performance comparable to the SOI counterparts, with propagation losses down to <0.1 dB/cm over the whole operational range [14–16]. Due to its dielectric nature, phase-shifter in SiN technology can rely only to the relatively slower thermo-optical modulation of the refractive index. Nevertheless, due to the large optical bandgap of $E_g > 4$ eV, SiN does not suffer EC or TPA losses, while nonlinear optical generation can still be significant owing to appreciable third-order nonlinearities. Stoichiometric silicon nitride (Si_3N_4) offers superior optical quality, however, the film thicknesses should be kept to less than 200 nm to avoid film

cracking due to the large tensile stress. This limitation can be overcome using sophisticated techniques, such as photonic Damascene [17] and multilayered TriPleX [15,18,19] processes.

An alternative approach to reduce film stress consists in introducing oxygen into the SiN material, by depositing directly a silicon oxynitride (SiON) film [20–23]. The refractive index of SiON can be continuously tuned between 1.45 (SiO₂) and 2.00 (Si₃N₄) by controlling the relative content of O and N in the film. The material loss can be lower than that of SiN in the visible and ultra-violet regions [24], meantime maintaining a very low stress for film thicknesses of up to few micrometers. As a drawback, the reduction of the material refractive index causes an increase in the device footprint, as well as a weakening of the thermo-optical and nonlinear optical characteristics of the guiding components [25].

In this work, we present a novel, low-loss, photonic platform based on SiON channel waveguides, capable to manage a wide range of VIS/NIR wavelengths for both linear and nonlinear optics applications. The core material consists in a relatively high refractive index SiON (1.66 at 850nm wavelength), which enables small footprint PIC designs with propagation losses ~ 1.5 dB/cm, improvable by at least a factor of two. The material shows an optical bandgap of 4.0 eV with a relatively strong optical nonlinearity of $1.3 \pm 0.6 \times 10^{-19}$ m²/W close to the TPA absorption edge. This, combined with the possibility to remove locally the cladding without damaging the waveguide, offers large versatility to engineer the waveguide dispersion for applications such as nonlinear Four-Wave Mixing (FWM) in ring resonator devices. Our SiON platform has the potential to be further developed for the monolithic integration of all necessary functionalities – photon sources, light manipulation circuits and photon detection (recently proven in Ref. [26]) – on a single chip, operating at room temperature, for classical and quantum applications.

2. Photonic platform

The photonic platform we introduce is based on the use of high-index SiON for the core material and SiO₂ claddings, resulting in a relatively large core/cladding index contrast of $\sim 15\%$. In addition, the channel waveguide is encapsulated between two thin films of Si₃N₄. These last act as an etch-stop barrier during the wet chemical etching, which is used to open windows in the waveguide's top SiO₂ cladding in specific locations on the chip, without the risk to underetch the bottom SiO₂ cladding. The removal of top SiO₂ is an optional process, which can be used for different purposes, for example, a chemical functionalization of the waveguide surface for sensing applications [22,27–30] or, as it will be discussed in Section 5, in cases when the refractive index dispersion of waveguides should be engineered for non-linear optics applications [31–36]. Furthermore, a conformal thin film of Si₃N₄ is expected to reduce the sidewall roughness of SiON waveguides, thus improving the propagation loss [37].

The fabrication process of the proposed platform is schematically described in Fig. 1. Starting from a 6 inch silicon wafer, first a 1.7 μm silicon oxide has been grown by wet thermal oxidation at 975 °C to form the bottom cladding. On top of it, a 50 nm thick Si₃N₄ is deposited in a Low-pressure chemical vapor deposition (LPCVD) furnace at 770 °C, followed by a 500 nm SiON film deposition in a plasma-enhanced chemical vapor deposition (PECVD) chamber using SiH₄, N₂O and NH₃ gas precursors. Next, the photonic devices were defined by photoresist patterning using an i-line stepper lithography, and the pattern transferred to the SiON/Si₃N₄ layers using reactive ion etching (RIE). Then, the SiON waveguides were thermally treated at 1050 °C for 90 min in a N₂ atmosphere to allow the release of residual H₂ and the improvement of the optical properties of the SiON film. Next, a second deposition of 50 nm Si₃N₄ was performed, followed by a deposition of LPCVD borophosphosilicate glass (BPSG) and PECVD SiO₂ films at 640 °C and 300 °C, respectively, to form the top cladding of a total of 1.6 μm .

In a next step, a multi-stack of 150 nm TiN and 1200 nm of Al was sputtered, patterned, and etched with RIE to allow for the realization of metal lines, contact pads and micro-heaters for the thermo-optical tuning of photonic components. The top Al film was selectively removed on top

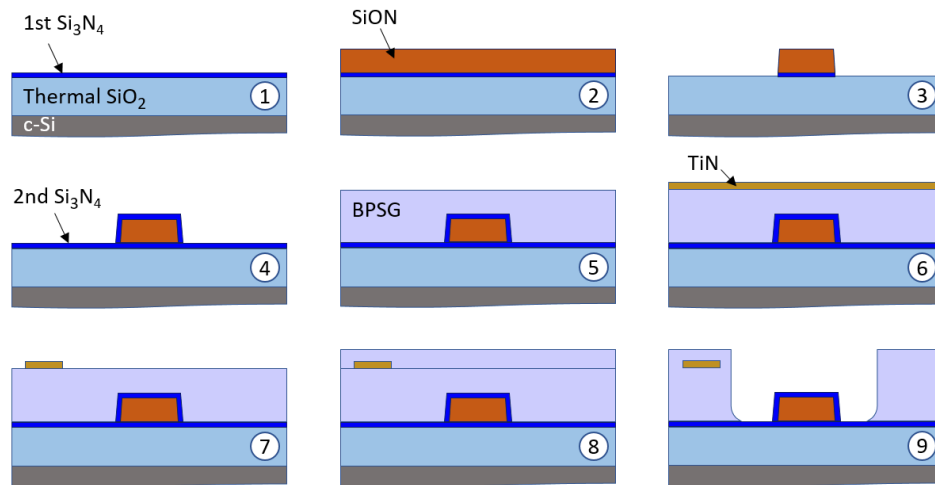


Fig. 1. Sketch of the fabrication process of the high-index SiON photonic platform. (1) The Si wafer with the bottom SiO₂ cladding and the Si₃N₄ film, (2) deposition of the SiON core material, (3) lithography and etching of waveguides, (4) deposition of the top Si₃N₄ film, (5) deposition of the top borophosphosilicate glass cladding (BPSG), (6) sputtering of the TiN film, (7) lithography and etching of the TiN resistors, (8) deposition of an oxidation protective film and (9) optional local opening of the waveguides top cladding.

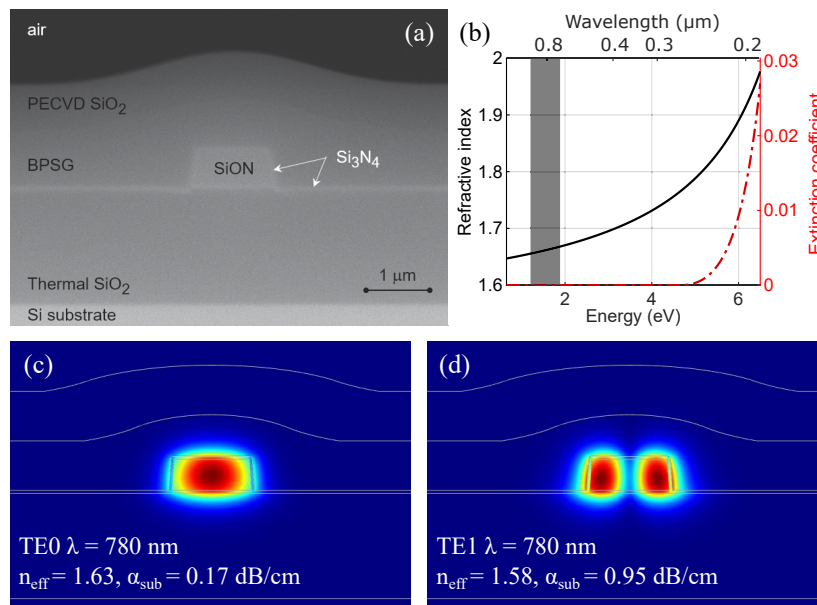


Fig. 2. (a) Cross-sectional SEM micrograph of a $1300\text{ nm} \times 500\text{ nm}$ SiON waveguide. The different materials of the multilayer composing the platform are labelled on the figure. (b) Dispersions for the real refractive index and the extinction coefficient of the SiON core material. The wavelength range of study for this work is highlighted in grey. Bottom: electromagnetic field distribution of the (c) TE₀ and (d) TE₁ modes of the waveguide showed in (a), with an indication of the simulated mode loss towards the silicon substrate.

of the micro-heaters, via wet chemical etching, in order to realize efficient TiN micro-resistances with a sheet resistance of $5 \Omega/\text{sq}$. The wafer was covered with 500 nm PECVD SiO_2 protective film, which was then removed from pad positions to allow for external electrical contact.

Finally, the chip boundaries and the waveguide facets were defined by RIE of the dielectric multilayer, with an additional 140 μm deep etch into the Si substrate through a Bosch process in order to ease the butt-coupling between optical fibers and waveguides. Figure 2(a) shows the SEM cross-sectional micrograph of the core of a 1300 nm \times 500 nm SiON waveguide. All the different films, including the surrounding 50 nm-thick Si_3N_4 , the bottom and top claddings as well as the Si substrate are clearly visible.

3. Linear properties

3.1. Material dispersion

The optical properties of the SiON films were characterized by variable-angle spectroscopic ellipsometry (VASE). The refractive index was modeled with the *New Amorphous* model based on the Forouhi-Bloomer dispersion equations [38]

$$n(E) = n_\infty + \frac{B_0 \cdot (E - E_0) + C_0}{(E - E_0)^2 + \Gamma_0^2}, \quad (1)$$

$$k(E) = \begin{cases} \frac{f_0 \cdot (E - E_g)^2}{(E - E_0)^2 + \Gamma_0^2} & \text{for } E > E_g \\ 0 & \text{for } E \leq E_g \end{cases}, \quad (2)$$

where E is the photon energy, n_∞ is the refractive index when $\omega \rightarrow \infty$, B_0 and C_0 contain the material characteristics

$$B_0 = \frac{f_0}{\Gamma_0} \cdot (\Gamma_0^2 - (E_0 - E_g)^2), \quad (3)$$

$$C_0 = 2 \cdot f_0 \cdot \Gamma_0 \cdot (E_0 - E_g). \quad (4)$$

This model allows to estimate the optical band gap E_g of the platform's core material. The parameters f_0 , Γ_0 and E_0 describe, respectively, the amplitude, the spectral width and the spectral position of the absorption peak in energy units. For our SiON material, the fitted parameters result in: $n_\infty = 1.56 \pm 0.03$, $E_g = 4.0 \pm 0.4$ eV, $f_0 = 0.07 \pm 0.02$, $E_0 = 7.8 \pm 0.8$ eV and $\Gamma_0 = 1.5 \pm 0.4$ eV (standard deviations from a sample of deposited films), which corresponds to factors $B_0 = -0.5 \pm 0.2$ eV and $C_0 = 0.8 \pm 0.3$ eV². The obtained dispersions for the refractive index and the extinction coefficient are plotted in Fig. 2(b).

Of particular interest for this work, the refractive index of SiON has been engineered to be higher than that of typical low-index SiON used in previous works [20,39,40]. This choice allows to design optical components with smaller footprint and larger optical mode confinement. Despite the relatively higher refractive index (1.66 at 850 nm), the estimated band-gap of $E_g \approx 4.0$ eV allows the photonic platform to be used without material absorption loss in the whole near-infrared and visible regions.

3.2. Propagation loss

Another important property to be optimized for a photonic platform is the propagation loss of waveguides, that can be attributed to several sources such as the material absorption, the radiative loss at bends, the loss towards the silicon substrate and the scattering due to surface roughness. The overall propagation loss per unit length can be characterized emulating the cutback method, by measuring the input/output power ratio of spiral-like waveguides of different lengths, as shown in Fig. 3.

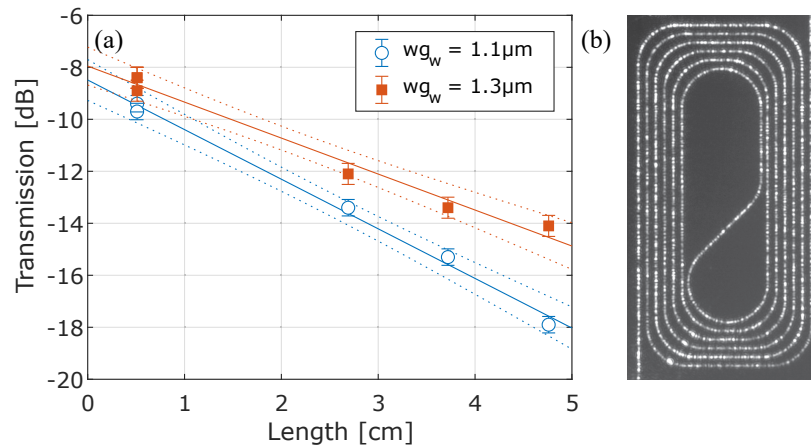


Fig. 3. (a) Measurement of the propagation losses α_{pro} through the cutback method at 780 nm wavelength for the TE polarization. Two different waveguide widths $wg_w = 1.1 \mu\text{m}$ (empty circles) and $1.3 \mu\text{m}$ (full squares) show $\alpha_{pro} = 1.8 \pm 0.1 \text{ dB/cm}$ and $1.5 \pm 0.1 \text{ dB/cm}$, respectively. Errorbars and dotted lines represent the standard deviation of the experimental data and the fit, respectively. (b) Optical image of a 2.7 cm long spiral waveguide under laser excitation.

This characterization was realized for two different widths of waveguides, namely $1.1 \mu\text{m}$ and $1.3 \mu\text{m}$, in the transverse-electric (TE) polarization. The analysis results a nearly flat response in the wavelength region 740 nm to 840 nm, with average propagation losses (α_{pro}) of $1.8 \pm 0.2 \text{ dB/cm}$ and $1.5 \pm 0.2 \text{ dB/cm}$ for the two widths, and a coupling loss (α_{cpl}) of $3.8 \pm 0.3 \text{ dB}$ per waveguide facet.

Within the proposed platform, the lowest propagation loss achievable with ideally smooth waveguides sidewalls is given by the loss α_{sub} toward the silicon substrate. The designed waveguides support both the first order (TE0) and the second order (TE1) modes, as shown in Fig. 2(c) and (d). However, the TE1 mode has a lower index contrast and is characterized by a higher substrate loss of $\alpha_{sub} = 0.95 \text{ dB/cm}$. For what concerns the TE0 mode, the ultimate propagation loss limit is fixed by simulation at $\alpha_{sub} = 0.17 \text{ dB/cm}$, with 1700 nm thickness of the bottom SiO_2 cladding. An increase of that thickness would allow to decrease, arbitrarily, the substrate loss. Yet, the proposed platform is intended to be monolithically integrated with silicon photodetectors into the substrate [26], which imposes a constrain for larger cladding thicknesses. The final 1700 nm thickness was selected as a balance between the two complementary needs.

4. Non-linear properties

The third-order optical nonlinearities of the SiON photonic platform have been studied by exploiting the phenomenon of Self-Phase-Modulation (SPM) [41,42]. An intense laser pulse, which propagates in a nonlinear medium, induces a local variation of the refractive index due to strong light-matter interactions. This variation causes a phase shift between the spectral components of the pulse resulting in a modulation of the pulse spectrum. Consequently, by measuring the spectral broadening of an ultra-short pulse with known power, one can retrieve the non-linear index of refraction n_2 of the material. In particular, following the split-step method described in Ref. [43], one can simulate the expected SPM effect for a given set of parameters, including: the material's n_2 coefficient, the waveguide geometry and the initial characteristics of the pulse. Then, by comparing the simulated results with the measured SPM spectra, the nonlinear index of the material can be estimated.

The SPM measurements were obtained using a mode-locked Ti:Sapphire laser, tunable in the wavelength range 720 nm-840 nm, with a 3-dB pulse-width of 0.2 nm (2 ps) and a repetition rate of 82 MHz. The laser is directly injected into the SiON waveguide using a lensed glass optical fiber. The transmitted pulse is collected with a second identical fiber at the waveguide output and analyzed in an Optical Spectrum Analyzer with 0.04 nm spectral resolution and sensitivity of -60 dBm.

The pulse-broadening experiment was performed for different input powers, ranging from 0 dBm to -20 dBm measured at the output of the waveguide, in order to verify the intensity dependence of SPM. Considering that the non-linear effects on the input pulse may occur also in the injection optics, composed of lenses and fibers, it is important to attenuate the power injected into the waveguides after the external optics. Therefore, the variation of the power coupled to the waveguide was realized by moving the input-fiber away from the waveguide's facet, to decrease the coupling efficiency. Figure 4 shows an example of the experimental data, obtained for two different pulses with central wavelengths at 780 nm and 840 nm.

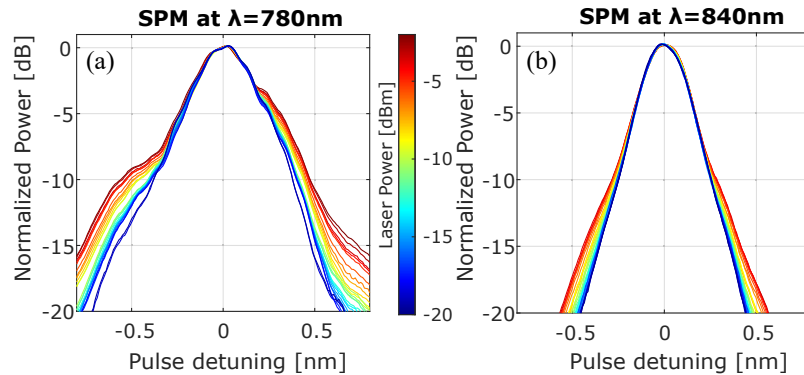


Fig. 4. Intensity-dependent spectral broadening of an ultra-short laser pulse induced by SPM effect in SiON waveguide for two different pulse wavelengths centered at (a) 780 nm and (b) 840 nm. The spectra are normalized to their peak powers. The difference in the input pulses lineshapes (the darkest blue lines) at the two central wavelengths is attributed to laser and table optics prior to interaction in the waveguides.

In order to estimate the unknown Kerr nonlinearity n_2 of the SiON material, we have performed numerical simulations which transform an input pulse spectrum into a broadened one. Having the knowledge of the waveguide's length and propagation loss, of the effective mode area (obtained by numerical simulations) and of the effective refractive index, the nonlinear Kerr coefficient can be then estimated according to the following procedure. For each set of measurements, the lowest-power signal is taken as the reference input pulse-shape. Then, for each power, a set of expected output signals are simulated with the split-step method for different values of n_2 (Fig. 5(a)). The final value of n_2 is thus estimated as the one that minimizes the spectral difference between the experimental data and the numerical solution (Fig. 5(b)). The main source of error in the estimation of n_2 within this approach is given by the error $\sigma_{\alpha_{tot}}$ of the total waveguide loss, given by the sum of propagation and coupling losses $\alpha_{tot} = \alpha_{pro} \cdot L + \alpha_{cpl}$, imposed in the numerical model. The uncertainty of the estimated n_2 was evaluated by simulating the spectra at three values of total waveguide loss: α_{tot} and $\alpha_{tot} \pm \sigma_{\alpha_{tot}}$, and by taking the difference $\delta n_2 = (n_2^{\max} - n_2^{\min})/2$ as the estimated error of n_2 .

The described numerical SPM simulations method is based on the experimental inputs, which account for the geometrical dimensions and linear optical properties of the fabricated waveguides. In order to verify the robustness of our approach, we applied this method to study a set of four

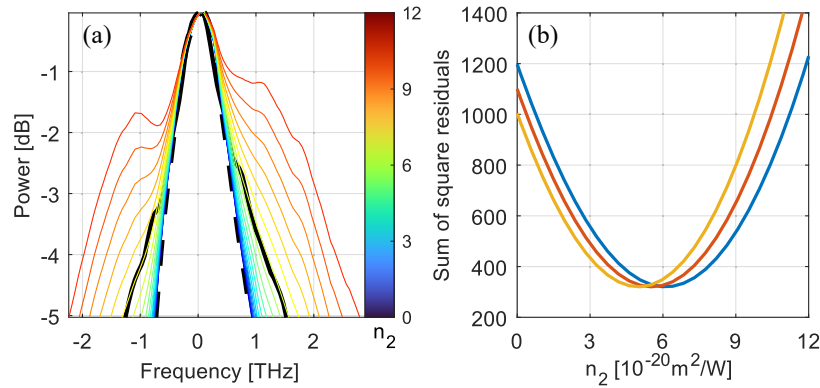


Fig. 5. Representation of the numerical fitting procedure to estimate the value of n_2 at wavelength of 840 nm. (a) Starting from the input pulse lineshape (dashed line), a set of output pulse lineshape was simulated for increasing values of the n_2 (blue to red, colorbar in units of $10^{-20} \text{ m}^2/\text{W}$), in order to match the experimental lineshape (black solid line). (b) Sum of the square residuals between the theoretical and the measured lineshapes. The minimum position corresponds to the optimal value of n_2 that gives the best fit to the experimental data. The n_2 estimations are obtained for three different values of the waveguides loss (propagation and coupling): α_{tot} , $\alpha_{tot} + \sigma\alpha_{tot}$ and $\alpha_{tot} - \sigma\alpha_{tot}$ (red, blue and yellow, respectively), in order to project the error on the measured loss to the error of estimated n_2 .

waveguides. In particular, a pair of waveguides was studied for two different nominal widths of 1100 nm and 1300 nm, as described in Table 1. The validation test, reported in Fig. 6(a), shows that at a fixed wavelength the estimations of n_2 are independent on the waveguide's geometry, within error, and therefore confirms the reliability of our analysis. The results are also consistent with previous works [25,44,45], indicating that the n_2 values of our SiON material are in between the expected values for pure SiO_2 and pure Si_3N_4 . The estimated nonlinear index corresponds to a nonlinear coefficient γ of $1.5 \text{ m}^{-1}\text{W}^{-1}$ at 780nm wavelength and $0.7 \text{ m}^{-1}\text{W}^{-1}$ at 840nm wavelength for the $1.1\mu\text{m}$ wide waveguides.

Table 1. Geometrical dimensions and estimated n_2 coefficients (in units of $10^{-20} \text{ m}^2/\text{W}$), at two different pump wavelengths, for the different investigated devices.

waveguide	width	length	n_2 (780 nm)	n_2 (840 nm)
wg A	$1.1\mu\text{m}$	27mm	13.1 ± 0.5	5.7 ± 0.4
wg B	$1.1\mu\text{m}$	37mm	13.5 ± 0.5	5.0 ± 0.4
wg C	$1.3\mu\text{m}$	27mm	12.3 ± 0.7	5.8 ± 0.5
wg D	$1.3\mu\text{m}$	37mm	13.5 ± 0.7	5.6 ± 0.5

In the following, we have selected one of the 1100 nm wide waveguides (sample A) and performed a spectral analysis of the variation of n_2 with wavelength. Figure 6(b) shows that the Kerr coefficient strongly increases while reducing the pump wavelength from Near-Infrared to Visible-Red region. This behavior is in accordance with the theoretical model that foresees a maximum in the nonlinear index located close to the TPA edge at $E_g/2$ [45], corresponding to a wavelength of about $\lambda_{\text{TPA}} \approx 310 \text{ nm}$ for our SiON platform.

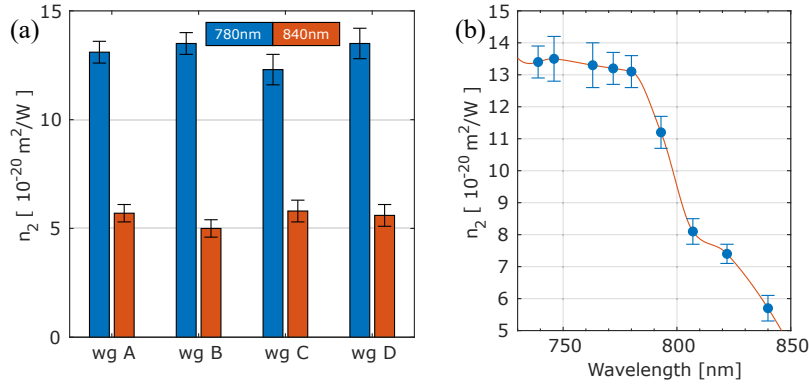


Fig. 6. (a) Results of n_2 estimation for different geometries of waveguides (see Table 1) at two different laser wavelengths: 780 nm (blue) and 840 nm (orange). The implemented analysis method allows to estimate n_2 values which are independent on the waveguide geometry, ensuring that the geometrical properties of the waveguides are weighted properly in the data analysis. (b) The measured spectral dispersion of the nonlinear refractive index n_2 . An increasing trend towards shorter wavelengths is clearly visible. Errorbars represent the half-interval $\delta n_2 = (n_2^{\max} - n_2^{\min})/2$ between the minimum and maximum values of n_2 estimated, for each waveguide, with different assumed waveguides loss as shown in Fig. 5.

5. Dispersion-engineered SiON ring resonators for generation of correlated photon pairs

The knowledge of the linear and non-linear properties of the developed SiON photonic platform makes it possible to engineer the modal refractive index, $n_{\text{eff}}(\omega)$, of the waveguide to match particular applications. Nonlinear schemes of generation of non-classical states of NIR photons often rely on SiN integrated microphotonic devices [33,36,46,47]. In this section, we describe our approach for the engineering of SiON-based ring resonator devices for on-chip generation of photon pairs via Spontaneous Four Wave Mixing (SFWM).

The dependence of n_{eff} on the light angular frequency leads to the dispersive nature of the mode's propagation constant $\beta(\omega) = n_{\text{eff}}(\omega) \cdot \omega/c$. For nonlinear wave interactions, of particular interest are the first two orders β_1 and β_2 of the Taylor expansion, representing the group index n_g and the Group Velocity dispersion (GVD):

$$\beta_1(\omega) = n_g/c = \frac{1}{c} \left(n_{\text{eff}} + \omega \frac{dn_{\text{eff}}}{d\omega} \right), \quad (5a)$$

$$\beta_2(\omega) = \frac{d\beta_1}{d\omega} = \frac{1}{c} \left(2 \frac{dn_{\text{eff}}}{d\omega} + \omega \frac{d^2 n_{\text{eff}}}{d\omega^2} \right). \quad (5b)$$

In a ring resonator, the group velocity β_1 defines the spectral separation δ_c between successive resonant modes – the *free-spectral range* (FSR) – following the relation $\delta_c = 1/(\beta_1 L_c)$, where L_c is the physical length of the cavity. A flat dispersion of $\beta_1(\omega)$ over a range of frequencies provides energy-equidistant cavity resonances, which is essential to fulfill the energy conservation requirement, for example, in nonlinear FWM and frequency comb generation experiments [36,46], where the pump, the signal and the idler should satisfy the relation $\omega_i = 2\omega_p - \omega_s$.

The parameter β_2 describes how the different spectral components of a propagating pulse travel, and in either case $\beta_2 > 0$ (*normal dispersion*) or $\beta_2 < 0$ (*anomalous dispersion*) result in temporal broadening of the pulse. The case of $\beta_2 = 0$ at some frequency – the zero dispersion frequency (ZDF) – is of particular interest for nonlinear optical applications because around

the ZDF different spectral components experience largely reduced second-order dispersion. In SFWM experiments with microring resonators around ZDF the spectral spread of δ_c is minimal and the flatness of n_g provides with larger nonlinear generation bandwidth [43,48].

We performed numerical axisymmetric simulations based on the Finite Elements Method in order to develop proper geometries for a device operating at NIR wavelengths, supporting single-mode characteristics and showing an anomalous GVD over the spectral range of interest. The radius of the studied ring resonators was set to 25 μm . This choice is motivated by the necessity to keep the ring radius large enough to avoid radiative losses but small enough to provide with $\delta_c \sim 1.12$ THz (2.4 nm), in order to minimize the spectral overlap of pump pulses with more than one mode of the resonator around 800 nm of wavelength.

First, we investigated a conventional geometry, in which the waveguide of a slightly trapezoidal form is fully embedded within the SiO_2 cladding (Fig. 7(a)). The lateral boundaries of the waveguide have an inclination angle of 86° , which is the typical value according to our fabrication process. The height of the SiON waveguide was fixed to 500 nm. Simulations were performed by varying the ring waveguide width from 900 nm to 1700 nm and the azimuthal number M of the fundamental radial mode from 270 to 360, covering a wavelength span of 200 nm around $\lambda = 850$ nm. The obtained results for the TE₀ mode showed that the GVD remains normal for all ring widths from 1100nm to 1300nm within the spectral range between 690 nm and 880 nm.

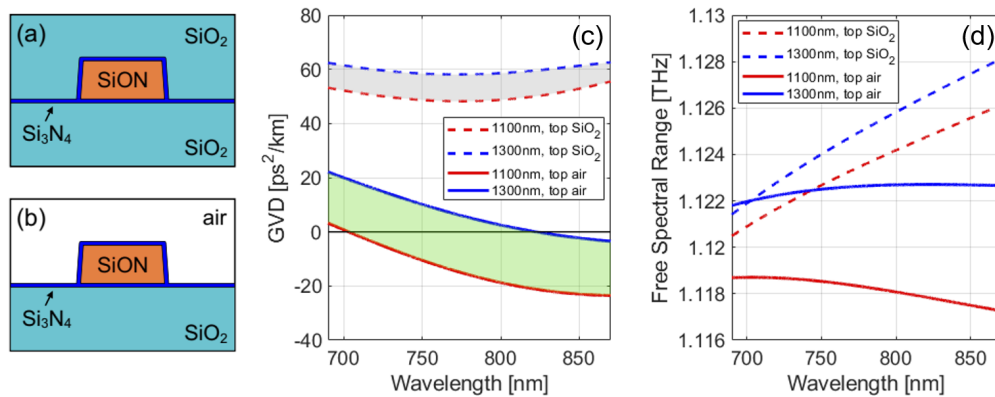


Fig. 7. (a) Sketch of the cross-sectional geometry of the SiON waveguide embedded in SiO_2 matrix. (b) The same geometry with the top SiO_2 cladding substituted with air. (c) The calculated GVD's of TE₀-modes for the respective geometries, showing that anomalous GVD can be achieved when the top SiO_2 cladding is substituted with air, with the ZDF depending on the waveguide width. (d) The calculated FSR of two rings evidences the sufficiently flat δ_c -trend for the air-cladded devices.

Next, we performed simulations of the same ring geometry substituting the top SiO_2 cladding with air (Fig. 7(b)). This new configuration turned to be particularly interesting since the GVD appeared to be much more sensitive to the variations of the waveguide width. We found that the GVDs of air-cladded resonators are already anomalous for smaller widths (~ 1100 nm) and turn slowly into a normal one over 1350 nm. In Fig. 7(c) we compare the calculated ring resonators GVDs for 1100 nm (red) and 1300 nm (blue) waveguide widths in both configurations with top SiO_2 (dashed line) and air-claddings (continuous line). The zero-dispersion point (ZDP) is observed at around $\lambda \approx 708$ nm for the 1100 nm waveguide width and around $\lambda \approx 822$ nm for the 1300 nm-wide one. We note that it is possible to engineer the waveguide width in order to achieve the ZDP in an arbitrary position inside this interval (green shaded area), in order to optimize the generation at the wavelengths where the material nonlinearity is higher (reported in Fig. 6). The air-cladded ring shows sufficiently flat dispersion of the group index and, consequently, a stable

FSR over a large span of wavelengths from 700 nm to 850 nm, depending on the waveguides width (Fig. 7(d)).

6. Conclusions

In this work, we have demonstrated a new silicon oxynitride-based integrated photonic platform for linear and nonlinear application in the VIS-NIR wavelength range. The fabricated devices show a low propagation loss <1.8 dB/cm, comparable to commercially available devices at 800 nm wavelength and with ongoing improvement of at least a factor two. We have demonstrated that, despite the reduction of the refractive index with respect to SiN, the SiON waveguides preserve a relatively strong optical nonlinearity of 13×10^{-20} m²/W around the wavelength 780 nm. Furthermore, thanks to the possibility to remove locally the cladding without damaging the waveguide, our platform allows for a larger versatility in engineering the waveguide dispersion. This enables to investigate one of the specific and peculiar applications of nonlinear FWM, by properly adjusting the group index and group velocity dispersion in order to enhance nonlinear photon pair generation in ring resonators. By combining the good linear properties, the promising optical nonlinearities for on-chip photon generation and our recently developed technology for on-chip photon detection [26], we envision the potential of this platform to achieve, in the near future, a full integration of photon generation sources, manipulation and detection on a single Silicon chip, operating at room temperature, for classical and quantum photonics applications.

Funding. European Commission (777222, 899368).

Acknowledgments. The authors are thankful to M. Bernard and G. Pucker for the fruitful discussions regarding the design and fabrication of the photonic devices.

Disclosures. The authors declare no conflicts of interest.

Data availability. Data underlying the results presented in this paper are not publicly available at this time but may be obtained from the authors upon reasonable request.

References

1. J. Capmany and D. Pérez, *Programmable Integrated Photonics* (Oxford University Press, 2020).
2. R. Osgood jr and X. Meng, *Principles of Photonic Integrated Circuits: Materials, Device Physics, Guided Wave Design* (Springer Nature, 2021).
3. S. Y. Siew, B. Li, F. Gao, H. Y. Zheng, W. Zhang, P. Guo, S. W. Xie, A. Song, B. Dong, L. W. Luo, C. Li, X. Luo, and G.-Q. Lo, "Review of silicon photonics technology and platform development," *J. Lightwave Technol.* **39**(13), 4374–4389 (2021).
4. W. Bogaerts and L. Chrostowski, "Silicon photonics circuit design: methods, tools and challenges," *Laser Photonics Rev.* **12**(4), 1700237 (2018).
5. N. M. Fahrenkopf, C. McDonough, G. L. Leake, Z. Su, E. Timurdogan, and D. D. Coolbaugh, "The aim photonics mpw: A highly accessible cutting edge technology for rapid prototyping of photonic integrated circuits," *IEEE J. Sel. Top. Quantum Electron.* **25**(5), 1–6 (2019).
6. T. Aalto, M. Cherchi, M. Harjanne, S. Bhat, P. Heimala, F. Sun, M. Kapulainen, T. Hassinen, and T. Vehmas, "Open-access 3- μ m soi waveguide platform for dense photonic integrated circuits," *IEEE J. Sel. Top. Quantum Electron.* **25**(5), 1–9 (2019).
7. M. R. Watts, W. A. Zortman, D. C. Trotter, R. W. Young, and A. L. Lentine, "Low-voltage, compact, depletion-mode, silicon mach-zehnder modulator," *IEEE J. Sel. Top. Quantum Electron.* **16**(1), 159–164 (2010).
8. H. Xu, X. Xiao, X. Li, Y. Hu, Z. Li, T. Chu, Y. Yu, and J. Yu, "High speed silicon mach-zehnder modulator based on interleaved pn junctions," *Opt. Express* **20**(14), 15093–15099 (2012).
9. O. Moutanabbir and U. Gösele, "Heterogeneous integration of compound semiconductors," *Annu. Rev. Mater. Res.* **40**(1), 469–500 (2010).
10. J. Brouckaert, G. Roelkens, D. Van Thourhout, and R. Baets, "Thin-film iii-v photodetectors integrated on silicon-on-insulator photonic ics," *J. Lightwave Technol.* **25**(4), 1053–1060 (2007).
11. G. Roelkens, L. Liu, D. Liang, R. Jones, A. Fang, B. Koch, and J. Bowers, "Iii-v/silicon photonics for on-chip and intra-chip optical interconnects," *Laser Photonics Rev.* **4**(6), 751–779 (2010).
12. D. J. Blumenthal, R. Heideman, D. Geuzebroek, A. Leinse, and C. Roeloffzen, "Silicon nitride in silicon photonics," *Proc. IEEE* **106**(12), 2209–2231 (2018).
13. T. J. Morin, L. Chang, W. Jin, C. Li, J. Guo, H. Park, M. A. Tran, T. Komljenovic, and J. E. Bowers, "Cmos-foundry-based blue and violet photonics," *Optica* **8**(5), 755–756 (2021).

14. D. J. Moss, R. Morandotti, A. L. Gaeta, and M. Lipson, "New cmos-compatible platforms based on silicon nitride and hydex for nonlinear optics," *Nat. Photonics* **7**(8), 597–607 (2013).
15. C. G. H. Roeloffzen, M. Hoekman, and E. J. Klein, *et al.*, "Low-loss Si₃N₄ triplex optical waveguides: Technology and applications overview," *IEEE J. Sel. Top. Quantum Electron.* **24**(4), 1–21 (2018).
16. J. Liu, G. Huang, R. N. Wang, J. He, A. S. Raja, T. Liu, N. J. Engelsens, and T. J. Kippenberg, "High-yield, wafer-scale fabrication of ultralow-loss, dispersion-engineered silicon nitride photonic circuits," *Nat. Commun.* **12**(1), 1–9 (2021).
17. M. H. Pfeiffer, A. Kordts, V. Brasch, M. Zervas, M. Geiselmann, J. D. Jost, and T. J. Kippenberg, "Photonic damascene process for integrated high-q microresonator based nonlinear photonics," *Optica* **3**(1), 20–25 (2016).
18. R. Heideman, A. Melloni, M. Hoekman, A. Borreman, A. Leinse, and F. Morichetti, "Low loss, high contrast optical waveguides based on cmos compatible lpcvd processing: technology and experimental results," in *Proc. of the 9th IEEE/LEOS Symp. in the Benelux*, (2005), pp. 71–74.
19. F. Morichetti, A. Melloni, M. Martinelli, R. G. Heideman, A. Leinse, D. H. Geuzebroek, and A. Borreman, "Box-shaped dielectric waveguides: A new concept in integrated optics?" *J. Lightwave Technol.* **25**(9), 2579–2589 (2007).
20. K. Wörhoff, A. Driessen, P. Lambeck, L. Hilderink, P. W. Linders, and T. J. Popma, "Plasma enhanced chemical vapor deposition silicon oxynitride optimized for application in integrated optics," *Sens. Actuators, A* **74**(1-3), 9–12 (1999).
21. R. Germann, H. Salemink, R. Beyeler, G. Bona, F. Horst, I. Massarek, and B. Offrein, "Silicon oxynitride layers for optical waveguide applications," *J. Electrochem. Soc.* **147**(6), 2237 (2000).
22. A. Samusenko, D. Gandolfi, G. Pucker, T. Chalyan, R. Guider, M. Ghulinyan, and L. Pavesi, "A silicon microring resonator-based platform for biosensing at 850 nm," *J. Lightwave Technol.* **34**(3), 969–977 (2016).
23. D. Chen, A. Kovach, X. Shen, S. Poust, and A. M. Armani, "On-chip ultra-high-q silicon oxynitride optical resonators," *ACS Photonics* **4**(9), 2376–2381 (2017).
24. C. Ance, F. De Chelle, J. Ferraton, G. Leveque, P. Ordejon, and F. Ynduráin, "Optical absorption in plasma-deposited silicon oxynitride films," *Appl. Phys. Lett.* **60**(11), 1399–1401 (1992).
25. A. Trenti, M. Borghi, S. Biasi, M. Ghulinyan, F. Ramiro-Manzano, G. Pucker, and L. Pavesi, "Thermo-optic coefficient and nonlinear refractive index of silicon oxynitride waveguides," *AIP Adv.* **8**(2), 025311 (2018).
26. M. Bernard, F. Acerbi, G. Paternoster, G. Piccoli, L. Gemma, D. Brunelli, A. Gola, G. Pucker, L. Pancheri, and M. Ghulinyan, "Top-down convergence of near-infrared photonics with silicon substrate-integrated electronics," *Optica* **8**(11), 1363–1364 (2021).
27. A. Densmore, M. Vachon, D.-X. Xu, S. Janz, R. Ma, Y.-H. Li, G. Lopinski, A. Delâge, J. Lapointe, C. C. Luebbert, Q. Y. Liu, P. Cheben, and J. H. Schmid, "Silicon photonic wire biosensor array for multiplexed real-time and label-free molecular detection," *Opt. Lett.* **34**(23), 3598–3600 (2009).
28. A. L. Washburn, L. C. Gunn, and R. C. Bailey, "Label-free quantitation of a cancer biomarker in complex media using silicon photonic microring resonators," *Anal. Chem.* **81**(22), 9499–9506 (2009).
29. H. Mukundan, A. S. Anderson, W. K. Grace, K. M. Grace, N. Hartman, J. S. Martinez, and B. I. Swanson, "Waveguide-based biosensors for pathogen detection," *Sensors* **9**(7), 5783–5809 (2009).
30. R. Heideman, M. Hoekman, and E. Schreuder, "Triplex-based integrated optical ring resonators for lab-on-a-chip and environmental detection," *IEEE J. Sel. Top. Quantum Electron.* **18**(5), 1583–1596 (2012).
31. A. C. Turner, C. Manolatu, B. S. Schmidt, M. Lipson, M. A. Foster, J. E. Sharping, and A. L. Gaeta, "Tailored anomalous group-velocity dispersion in silicon channel waveguides," *Opt. Express* **14**(10), 4357–4362 (2006).
32. S. Mas, J. Caraquitena, J. V. Galán, P. Sanchis, and J. Martí, "Tailoring the dispersion behavior of silicon nanophotonic slot waveguides," *Opt. Express* **18**(20), 20839–20844 (2010).
33. H. Zhao, B. Kuyken, S. Clemmen, F. Leo, A. Subramanian, A. Dhakal, P. Helin, S. Severi, E. Brainis, G. Roelkens, and R. Baets, "Visible-to-near-infrared octave spanning supercontinuum generation in a silicon nitride waveguide," *Opt. Lett.* **40**(10), 2177–2180 (2015).
34. Y. Zhang, J. Zou, and J.-J. He, "Temperature sensor with enhanced sensitivity based on silicon mach-zehnder interferometer with waveguide group index engineering," *Opt. Express* **26**(20), 26057–26064 (2018).
35. K. Guo, J. B. Christensen, X. Shi, E. N. Christensen, L. Lin, Y. Ding, H. Ou, and K. Rottwitz, "Experimentally validated dispersion tailoring in a silicon strip waveguide with alumina thin-film coating," *IEEE Photonics J.* **10**(1), 1–8 (2018).
36. Y. Zhao, X. Ji, B. Y. Kim, P. S. Donvalkar, J. K. Jang, C. Joshi, M. Yu, C. Joshi, R. R. Domenegueti, F. A. S. Barbosa, P. Nussenzeig, Y. Okawachi, M. Lipson, and A. L. Gaeta, "Visible nonlinear photonics via high-order-mode dispersion engineering," *Optica* **7**(2), 135–141 (2020).
37. M. W. Puckett, K. Liu, N. Chauhan, Q. Zhao, N. Jin, H. Cheng, J. Wu, R. O. Behunin, P. T. Rakich, K. D. Nelson, and D. J. Blumenthal, "422 million intrinsic quality factor planar integrated all-waveguide resonator with sub-mhz linewidth," *Nat. Commun.* **12**(1), 934 (2021).
38. A. Forouhi and I. Bloomer, "Optical properties of crystalline semiconductors and dielectrics," *Phys. Rev. B* **38**(3), 1865–1874 (1988).
39. G.-L. Bona, R. Germann, and B. J. Offrein, "Silicon high-refractive-index waveguide and planar lightwave circuits," *IBM J. Res. Dev.* **47**(2.3), 239–249 (2003).

40. D. Chen, A. Kovach, S. Poust, V. Gambin, and A. M. Armani, "Normal dispersion silicon oxynitride microresonator kerr frequency combs," *Appl. Phys. Lett.* **115**(5), 051105 (2019).
41. R. H. Stolen and C. Lin, "Self-phase-modulation in silica optical fibers," *Phys. Rev. A* **17**(4), 1448–1453 (1978).
42. N. Tzoar and M. Jain, "Self-phase modulation in long-geometry optical waveguides," *Phys. Rev. A* **23**(3), 1266–1270 (1981).
43. G. P. Agrawal, "Nonlinear fiber optics," in *Nonlinear Science at the Dawn of the 21st Century*, (Springer, 2000), pp. 195–211.
44. K. Ikeda, R. E. Saperstein, N. Alic, and Y. Fainman, "Thermal and kerr nonlinear properties of plasma-deposited silicon nitride/silicon dioxide waveguides," *Opt. Express* **16**(17), 12987–12994 (2008).
45. M. Sheik-Bahae, D. J. Hagan, and E. W. Van Stryland, "Dispersion and band-gap scaling of the electronic kerr effect in solids associated with two-photon absorption," *Phys. Rev. Lett.* **65**(1), 96–99 (1990).
46. R. Cernansky, F. Martini, and A. Politi, "Complementary metal-oxide semiconductor compatible source of single photons at near-visible wavelengths," *Opt. Lett.* **43**(4), 855–858 (2018).
47. X. Lu, Q. Li, D. A. Westly, G. Moille, A. Singh, V. Anant, and K. Srinivasan, "Chip-integrated visible–telecom entangled photon pair source for quantum communication," *Nat. Phys.* **15**(4), 373–381 (2019).
48. I. H. Agha, Y. Okawachi, and A. L. Gaeta, "Theoretical and experimental investigation of broadband cascaded four-wave mixing in high-q microspheres," *Opt. Express* **17**(18), 16209–16215 (2009).